NRIAG JOURNAL OF ASTRONOMY AND GEOPHYSICS
2019, VOL. 8, NO. 1, 73–83
https://doi.org/10.1080/20909977.2019.1615802

Tectonics mapping using geophysical data around Nuweiba area, Gulf of Aqaba, Sinai, Egypt

Sultan Awad Sultan Araffa[a], Hassan Saleh Sabet[b] and Mohammed Hussien Mahmoud[b]

[a]National Research Institute of Astronomy and Geophysics (NRIAG) Helwan, Cairo, Egypt; [b]Geology Department, Faculty of Science, Al Azhar University, Cairo, Egypt

ABSTRACT

The main target is to delineate the structural features and tectonic hazard for the study area. Three geophysical tools that are used to configure the tectonic setting in the study are gravity, magnetic and seismic activity. Gravity measurements were acquired to represent about 201 gravity stations covered the studied area. Different gravity corrections such as drift, tide, latitude, free-air, Bouguer and Terrain corrections were performed using the commercial software Oasis Montaj version 8.3. The interpretation of gravity data indicates that different trends of structures, for example, NW-SE, N–S and NE–SW trends where most of these fault elements are active faults according to seismic events which were recorded on their locations. Also, 201 land magnetic stations were measured at same sites of gravity stations. The basement depth derived from the magnetic data has value between 744 m and 4122 m.

KEYWORDS

Euler; rose diagram; subsurface structures; gravity; magnetic; seismicity

1. Introduction

Sinai Peninsula occupies the far northeastern corner of Egypt. It is considered as one of the fifth main geographical provinces of Egypt with Nile Valley, Nile Delta, Western Desert, Eastern Desert, and Sinai Peninsula. The Sinai Peninsula lies between latitudes 27°45′ N and 31°30′ N and longitudes 32°00′ E and 35°00′ E, it covers an area of about 61,000 km^2, which represents 6% of the total area of Egypt. It represents the frontier border between Egypt and Palestine. (Said 1990).

The studied area lies at the southern part of Sinai, Egypt, between Nukhil and Katherina, bounded from the west by the Gulf of Seuz, from the east by the Gulf of Aqaba (Figure 1(a)). It is located between Latitudes 28° 45′ and 29° 45′ N and longitudes 33° 45′ and 34° 45′ E. It represents an area of about (6706 Km^2). The area under study investigated by many geophysicists such Ibrahim et al. (2004), Monteiro Santos et al. (2006) and Sultan et al. (2009), Araffa, et al. (2015) to delineate the structures and groundwater optionality. Also, the present study aims to delineate the structures which have been direct effect on the configuration of groundwater aquifers, defining the basins which can be reservoirs for oil accumulations and detecting the active faults which can be act as a factor on the distribution of population through the damage of many of constructions in the studied area. The results of interpretation of geophysical data can be used to select the safe sites for new construction far from the sites of high seismic activity. These targets can be solved through the results of potential data (gravity, magnetic) and seismic data in the investigated area.

2. Geological setting

2.1. Geomorphology

Different geomorphologic studies on the studied area were carried out by many authors such as Ball (1916), Beadnell (1926), Abdallah and Abu Khadrah (1977), and Hammad (1980).

Abdallah and Abu Khadrah (1977) partitioned Sinai into five geomorphic units. The southern mountain unit, Tih-Egma unit, the conspicuous hilly unit, the Mediterranean coastal zone, and the western part of Suez Gulf coastal zone (Figure 1(b)).

2.2. Surface geology

The surface geology has been described through a geological map of Sinai at a scale of 1:500,000 performed by UNSECO Cairo Office (2005) (Figure 1(c)). The area is mostly covered by Pleistocene Age made out of alluvium deposits and Paleocene deposits including Esna Shale Formation, which is formed of greenish marly shale. Successive geological formations from the Lower Eocene to Upper Cretaceous cover the eastern part of the area under study. The Egma Formation of chalky limestone represents the Lower Eocene succession. The Upper Cretaceous is represented by Sudr Formation, which is consists of chalk of Maastrichtian age – the Duwai Formation made out

CONTACT Sultan Awad Sultan Araffa sultan_awad@yahoo.com National Research Institute of Astronomy and Geophysics (NRIAG)

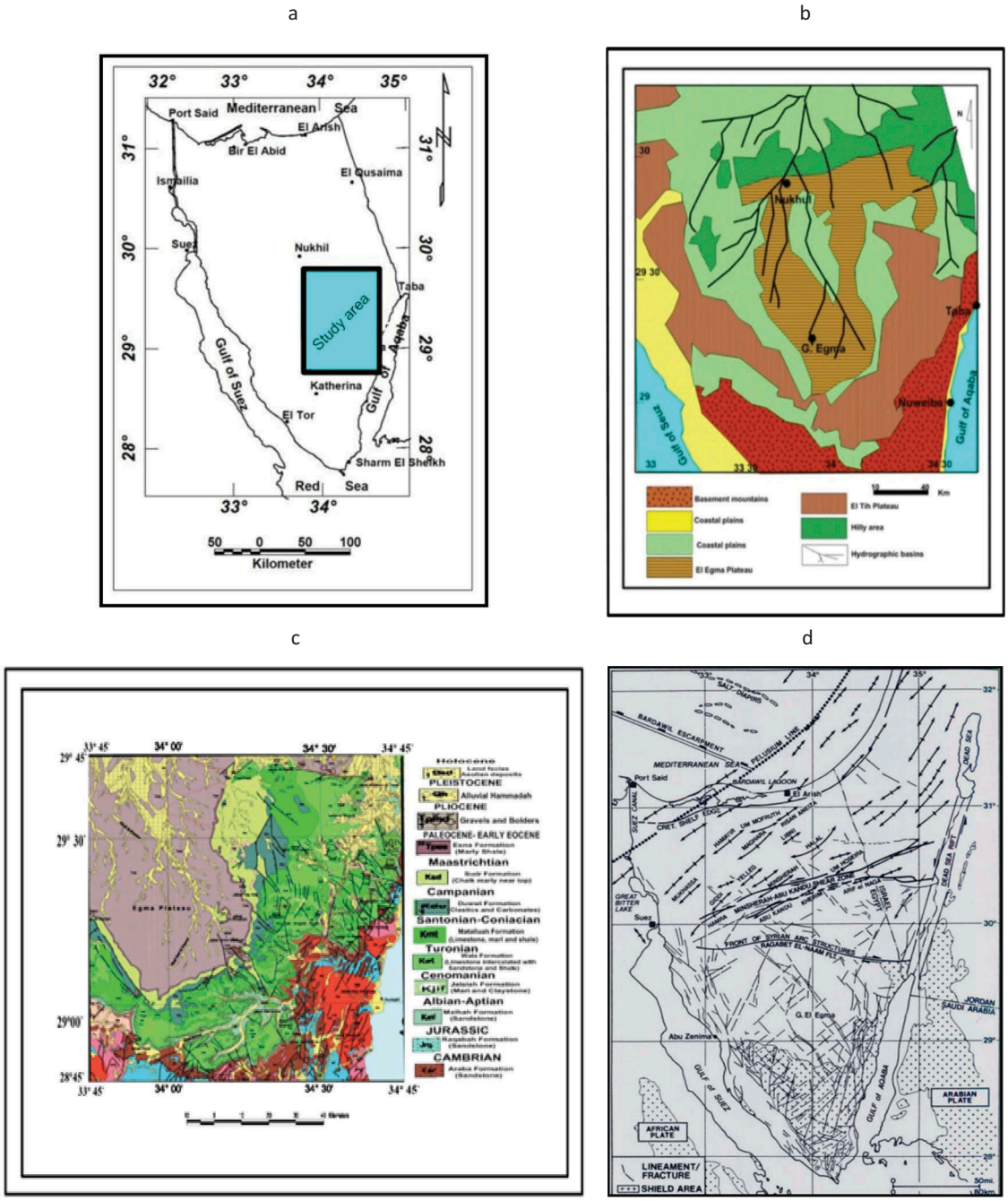

Figure 1. (a) Location map of the studied area, (b) Geomorphic map of Sinai (after Abd Allah and Abu Khadrah, 1977), (c) Geologic map of the studied area (modified after UNSECO Cairo Office 2005), (d) Tectonic map of Sinai Peninsula (after Neev 1975 and Agah, 1981).

of alternate beds of clastic and carbonates, with phosphatic bands and pockets of Upper Cretaceous age – the Matullah Formation, which is formed of clastic sequence with limestone and dolomite strata and the Wata Formation, composed of dark yellow to brown glauconitic Sandy limestone interbedded with marly dark green shale and cross bedded mudstone (Upper Cretaceous; Hassanin, 1997).

2.3. Mapped faults

The studied area is affected by many faults. According to Said (1990), and Zaghloul (1983) summarised the fault system affected Sinai into five groups: Meridional trend, Pelusium trend, Aqaba-Dead Sea trend, Alexandria trend and Clysmic (Erythrean) trend. In central Sinai, Gebel El Tih-Egma plateau 914 m above sea level represents a thin sedimentary cover which is affected by faulting. This region has been described in detail by Shata (1956). Some wadies follow the fault lines, and faults may represent either barriers to the movement of groundwater, as Raqabet El Naam fault, or a recharge boundary to the aquifer closer to the fault (Al Abassy 2010) (Figure 1(d)).

3. Gravity measurements and interpretation

3.1. Gravity data acquisition

Gravity data has been acquired by the CG-3 Gravimeter through 201 land stations arranged in a grid-like pattern, 3000 m apart, to cover the sensitivity whole area of 0.01 mGal (Figure 2(a)). The values of measured gravity were corrected to corrections of different gravity like drift, tide, freeair, Bouguer, latitude, and topographic corrections using specialised software (GM-SYS Programs 2007). The corrected gravity values were used to plot Bouguer anomaly map using GM-SYS Programs (2007) as represented in Figure 2(b). It shows anomalies of high-gravity (−0.4 m Gal) at N, E, SW and central parts, but SE part and some places S, NE, E and central parts reveals low gravity anomalies (−63.7 mGal). The low Bouguer anomalies indicate thick sedimentary successions, in contrast the high gravity anomalies caused by uplifts of basement rocks. These rock bodies are isolated by major structural lines that are mainly faults. Thus, an increase in the thickness of the sedimentary rocks is bounded by elevation of the denser and older basement rocks.

3.2. Gravity interpretation

The interpretation of gravity data stated with gravity separation where the technique high pass and low pass was applied for the gravity separation. The high and low pass filter technique was applied by using the Energy (Power) Spectrum (Wingograd 1978) at wave number of 0.018 km (Figure 3(a)). The depth of deep sources is about 5.9 Km and the depth of shallow sources is about 2.7 Km from the next equation:

H = -S/4π Where H = depth and S = slope of the log (energy) spectrum.

3.2.1. Gravity separation

The regional-residual separation technique was carried out to filter; the regional component was related to deep seated sources, and residual component was related to local sources. In the present study authors used technique high pass, low pass to apply the gravity separation. The high and low pass filter technique with a cut wave number cut-off of 0.018 km−1 was applied to the Bouguer anomaly map to calculate the regional and residual maps. The resulted of high-pass filter map shows that the gravity anomaly field in the studied area has a maximum value (35.5 mGal) at N, E part which have coordinates between long.34°30′ E and long.34° 35′ E and between lat.29°15′ N and lat.29°30′ N, W part which have coordinates between long.34°05′ E and long.34°10′ E and between lat.28°55′ N and lat.29°10′ N, central part of studied area which have coordinates between lat.28°50′ N and lat.29°15′ N and between long.34°15′ E and long.34°35′ E and SW part of the studied area. and a minimum value (−21.3 mGal) at NE part, SW part, S part, E part which have coordinates between long.34°30′ E and long.34°35′ E and between lat.28°50′ N and lat.29°20′ N and central part of studied area which have coordinates between lat.29°15′ N and lat.29°25′ N and between long.34°10′ E and long.34°30′ E of the studied area. Most of the anomalies are seen as trending in E-W, N -S and NW-SE directions (Figure 3(b)).

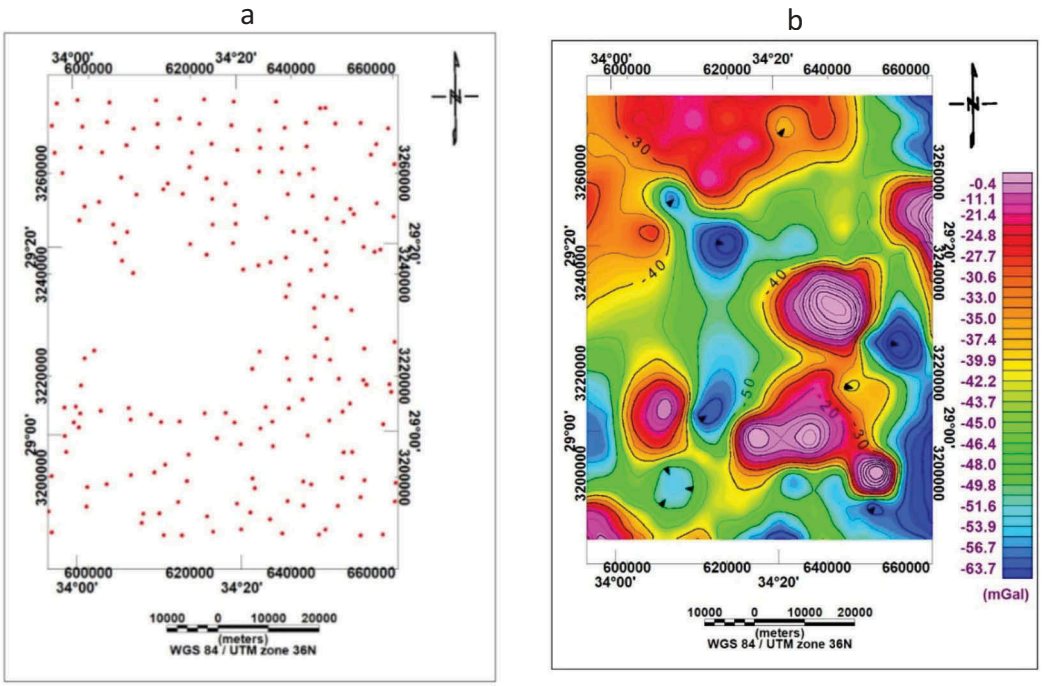

Figure 2. (a) Gravity stations in the studied area, (b) Bouguer anomaly map of the studied area.

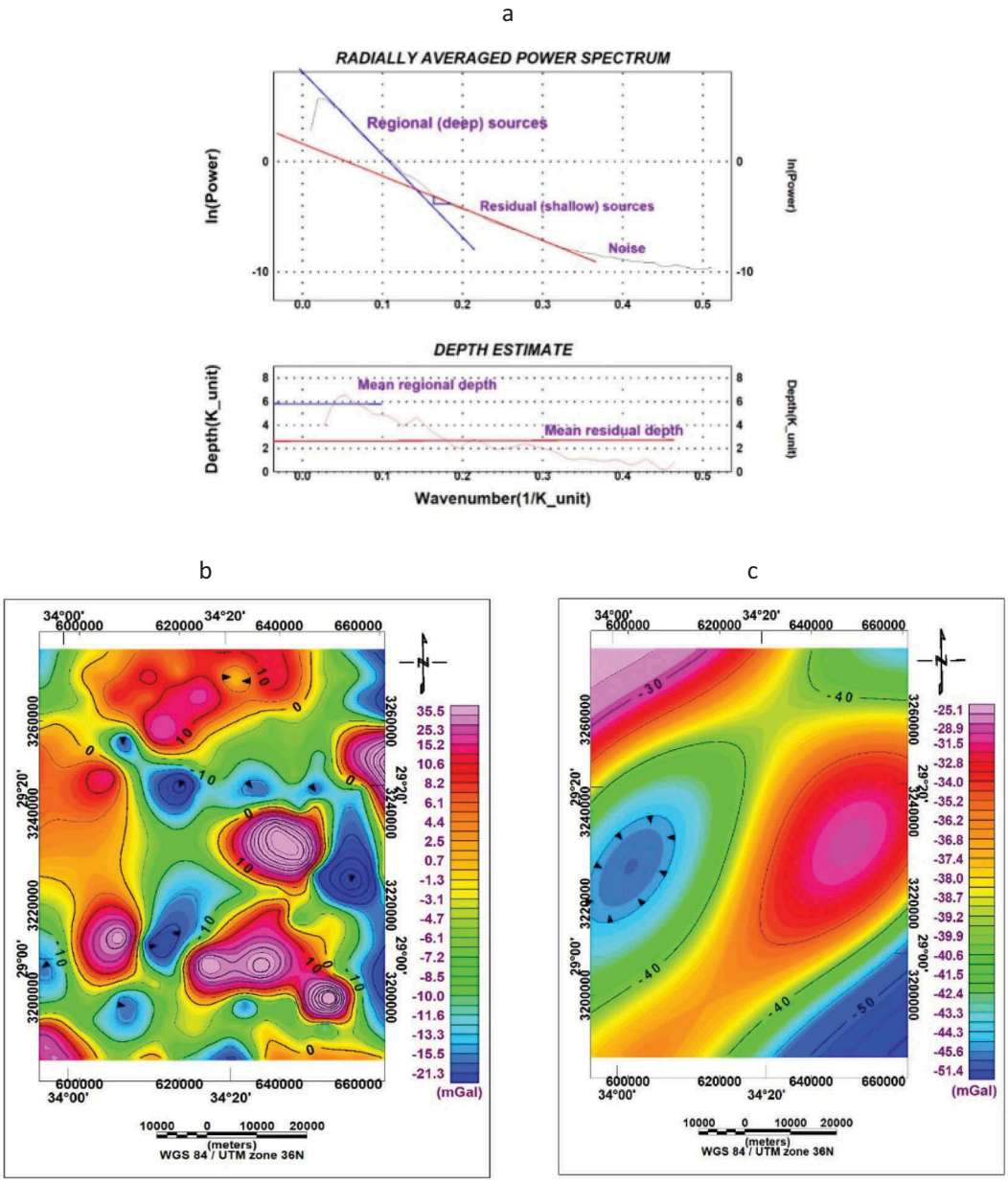

Figure 3. (a) Power spectrum of gravity data showing the corresponding averaging regional and the residual, (b) Regional Bouguer anomaly map and b residual Bouguer anomaly map using a low- and high-pass filter with a cut wave number of 0.018 km^{-1}.

The results of low-pass filter map show that the gravity anomaly field in the area ranges between a maximum value (−25.1 mGal) at NW, E and SW parts of the studied area and a minimum value (−51.4 mGal) at west and SE parts of the studied area. All of the anomalies are seen as half trending in NE-SW directions (Figure 3(c)). The high gravity anomaly is mainly due to uplift of denser basement rock, while the lower gravity values indicate sedimentary basins.

3.2.2. Euler deconvolution

Euler deconvolution is used to determine the depth of source of anomaly and structural index of a list of anomalies (Thompson 1982). The Euler deconvolution process is applied at each solution. The best solutions which make the results are concentrated at some places in the studied area "not distributed all over the area".

In the present study the structural index which applied are 0, 1 and 2 to select the best solution on the residual gravity anomaly map at SI = 0 as in (Figure 4 (a)), SI = 1 as in (Figure 4(b)), and SI = 2 as in (Figure 4 (c)). The structural index (0) gives better solution than structural index 1 and 2, because the data are concentrated at some places in the studied area not distributed all over the area as SI = 1 and SI = 2. The best solution at SI = 0 which indicate on many structures as sill, Dyke, Ribbon, and step structure in the studied area.

The Euler map shows the depth ranges from lower than 500 m to greater than 5000 m.

3.2.3. Delineating of structure elements

The residual Bougeur anomaly map was interpreted to delineate the common structural trends affecting the studied area. The detected lineaments on the map

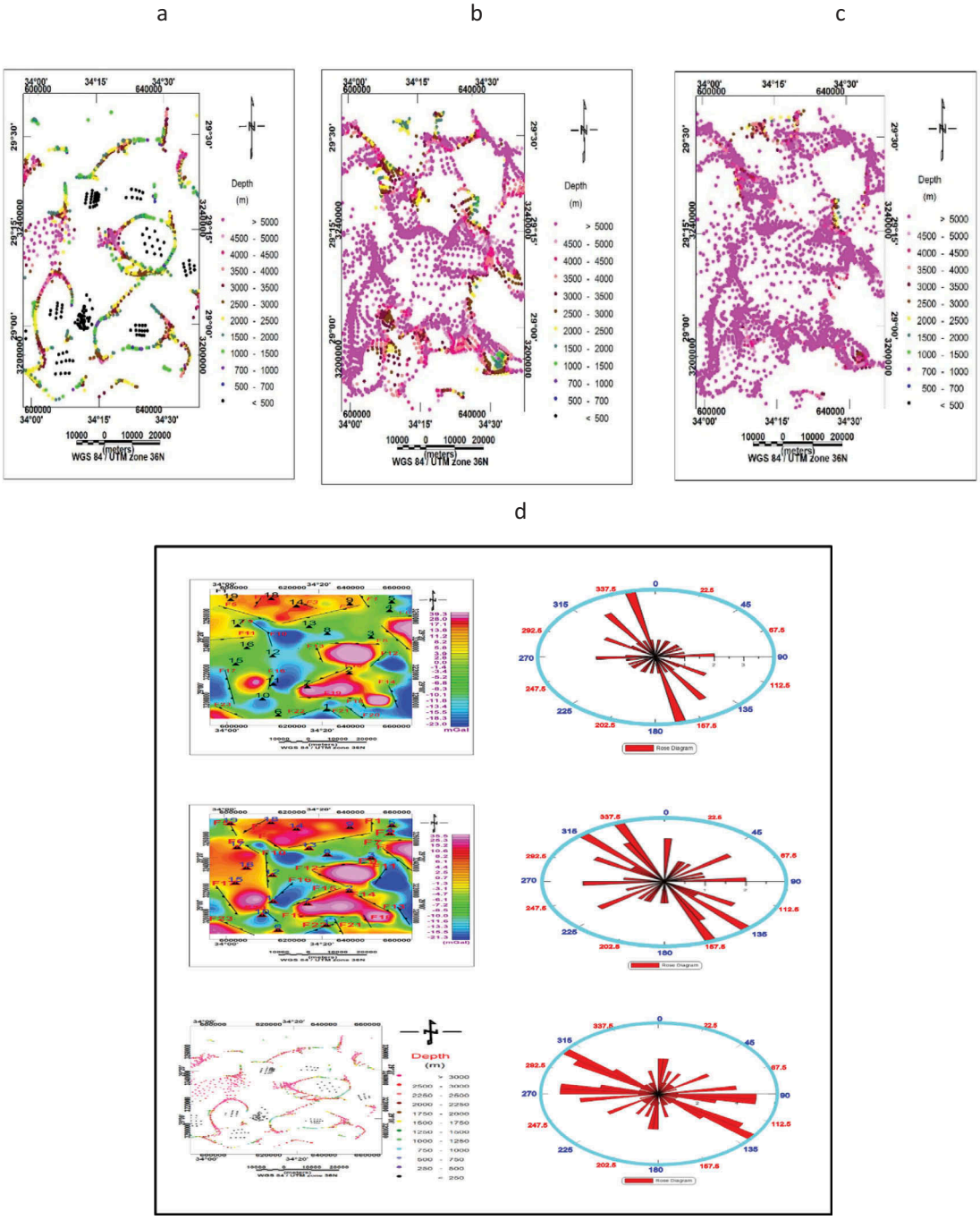

Figure 4. (a) Euler solutions of structural index = 0, (b) Euler solutions of structural index = 1, (c) Euler solutions of structural index = 2, (d) Fault elements dissecting the studied area from gravity interpretation, h pass and Euler solutions with structural index zero and Major trend faults dissecting the studied area.

represent the inferred faults and/or contacts of different rock types of varied lengths and directions. These lineaments were measured clockwise from north, statistically analysed and plotted in the form of rose diagrams, which is a member of the rock Ware Utilities Package, as shown in Figure 4(d). About 23 faults were determined to cross the studied area. These faults take different trends N-S, E-W, NE-SW, and NW-SE and are numbered in Figure 4(d).

The faults No. F1, F4, F10, F13, F14, F16, F17 and F18 have nearly N-S trend.

The faults No. F1, F10, F14 and F16 have downthrown towards the east.

The faults No. F4, F13, F17 and F18 have downthrown towards the west.

The faults No. F3, F5, F7, F9, F20, F21 and F23 have NW-SE trend.

The faults No. F3, F9, F20 and F23 have downthrown NE trend.

The faults No F5, F7 and F21 have downthrown SW trend.

The faults No. F2, F12, F15 and F22 have NE-SW trend.

The faults No. F2, F12 and F22 have downthrown SE trend.
The fault No. F15 has down through NW trend.
The faults No. F6, F8, F11 and F19 have E- W trend.
The faults No. F6 and F8 have downthrown towards the north.
The faults No. F11 and F19 have downthrown towards the south.

The directions of faults are represented in the rose diagram (Figure 4(d)). It's clear that the major direction is NW-SE (parallel to Gulf of Suez direction).

4. Magnetic measurements and interpretation

201 ground magnetic stations have been measured to cover the studied area, using Envimag proton magnetometer (model Scintrex) of sensitivity 1nT. The measurements are carried out at stations spaced every 2–3 kms in the studied area. Two instruments used for measurements, one for field work measurements and the other one for base station recording to estimate diurnal variation correction. Magnetic data corrections are applied for measured data, diurnal variation correction and IGRF corrections are applied and corrected data are contoured by using Oasis Montaj Programs, 2015 to produce the total intensity magnetic map.

4.1. Qualitative analysis of the magnetic data

4.1.1. Total intensity magnetic map

The original total intensity magnetic map (Figure 5(a)) was divided into two zones, the first zone is high-frequency anomalies present in the western, northern, and southeastern parts of the map ranging from 42364.9 to 42552.9 nano Tesla and could be related to shallow subsurface magnetic sources and appear as elongated shape, this anomaly takes trends E-W and NW-SE directions. The second zone is low-frequency anomalies seen in the eastern, southwestern and southern parts of the map ranging from 42171 to 42277.9 nano Tesla, takes trends E-W and some anomalies distributed in northwestern corner, this anomaly takes direction NW-SE and some anomalies distributed in the central part.

4.1.2. Magnetic map reduced to the pole

In the present study, the total intensity magnetic map reduced to the magnetic pole (Figure 5(b)) has been calculated automatically by using GM-SYS Programs (2007) by input of the programme parameters as inclination (43.157), declination (3.34), magnetic field strength (43076.1600 gammas) and of the instrument sensor from the ground surface (l m).

4.1.3. Downward continuation

The downward continuation method was applied to represent RTP map at different depths. Nine downward continuation maps were constructed by using

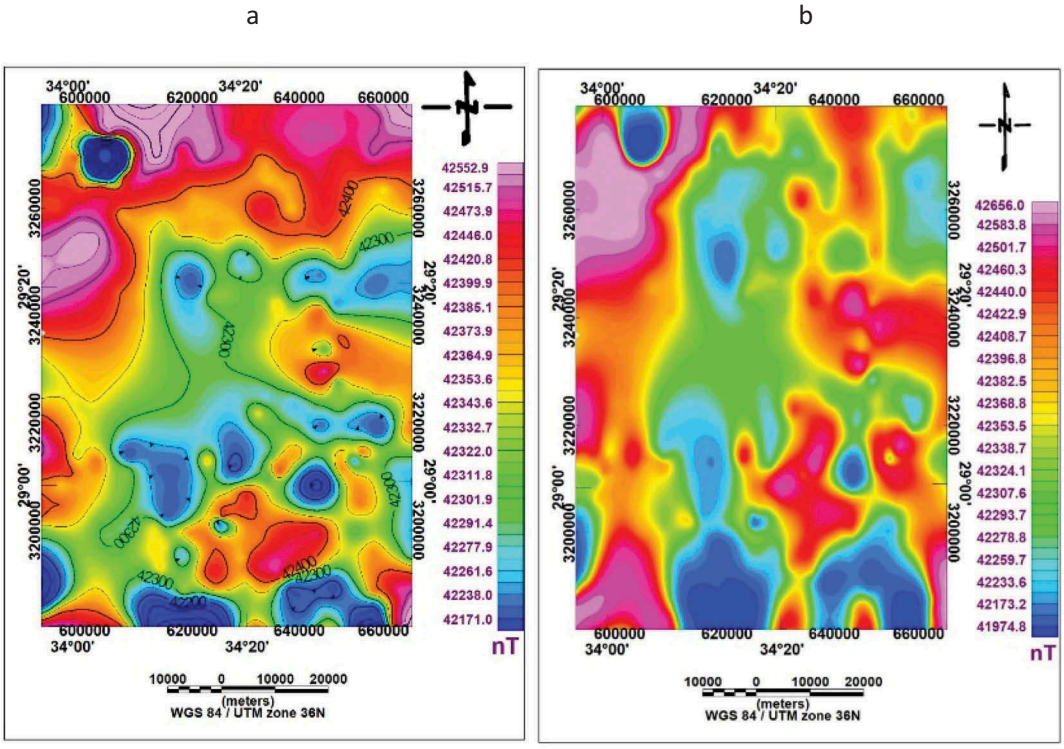

Figure 5. (a) Total intensity magnetic map, (b) Total intensity magnetic map reduced to the Pole (RTP map).

grid spacing 100, 200, 500, 800, 1000, 1500, 2000, 3000 and 4000 m (Figure 6(a)).

In these maps, the anomalies start in splitting by reaching the depth 800 m; this may indicate that the top of the source bodies lie near this level. By reaching to level 4000 m, the anomaly is completely distorted; this may indicate that the base of source bodies lie near this level.

4.1.4. Upward continuation

A group of upward continuation maps have been constructed to get rid of the residual sources and reaching at the more convincing regional surface that confirms the regional map obtained via separation process. Nine maps at 100 m, 200 m, 500 m, 800 m, 1000 m, 1500 m, 2000 m, 3000 m and 4000 m in depth were applied to construct upward continuation filters. They illustrate the change in anomaly character with increasing observation to source distance. Inspection of the upward continuation maps (Figure 6(b)) show great similarity in their characters with RTP anomaly map; this may indicate that most of the anomalies come from deep source

4.1.5. Horizontal derivatives

Horizontal-gradient maps are vivid yet manageable and inherent derivative outputs to explain the anomaly texture of potential-field maps and to highlight discontinuities in the anomaly pattern.

In one dimension, horizontal derivative can be accomplished in the space domain by subtracting the first value from the third one or by subtracting two respective values; the resultant value will describe the point midway between these two values

$$\frac{\mathrm{df(x)_1.5}}{\mathrm{dx}} = [\mathrm{f(x\_2)} - f(\mathrm{x\_1})]/\Delta x \tag{1}$$

$$\frac{\mathrm{df(x)_2}}{\mathrm{dx}} = \frac{[F(\mathrm{x_3}) - F(\mathrm{x_1})]}{2\Delta \mathrm{x}} \tag{2}$$

4.1.5.1. Horizontal derivatives maps. The horizontal derivatives maps in both X and Y directions are generated in the present study (Figure 7(a–d)) obtained from the RTP data of the studied area.

The first horizontal derivative in X-direction maps (Figure 7(a)) reveals that the main structural trends dominating Nuweiba area are the N-S and NW – ES directions.

On the other hand, the first horizontal derivative in the Y-direction (Figure 7(b)) explains that the most effective trends are E-W and NW – ES directions.

The second horizontal derivative in X-direction maps (Figure 7(c)) reveals that the main structural trends dominating Nuweiba area is the N-S direction.

On the other hand, the second horizontal derivative in the Y-direction (Figure 7(d)) explains that the most effective trend is E-W direction.

4.1.6. Vertical derivatives

This technique is designed to highlight the locations of fault and contact features. The first vertical derivatives can be mathematically determined from the total magnetic field anomaly map. The first vertical derivatives represent as a sharper resolution of near-surface features. The vertical derivative can be calculated by taking average values over circles at different distances from a

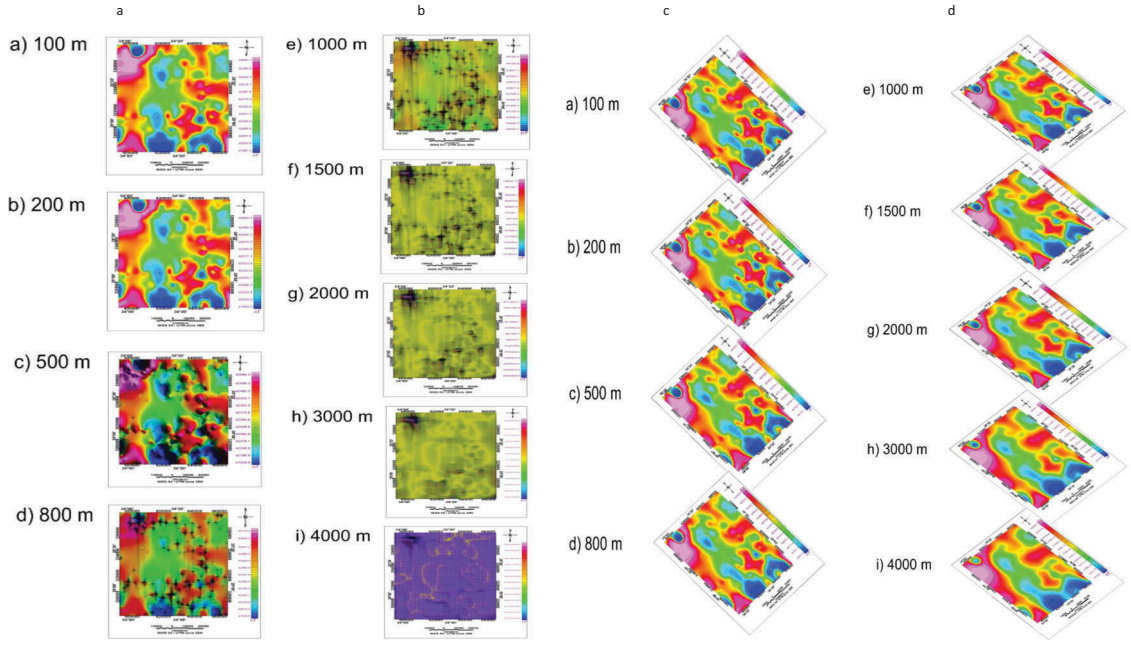

Figure 6. Part1: represents the downward continuation at distances 100, 200, 500, 800, 1000, 1500, 2000, 3000 and 4000 m, Part2: represents the upward continuation at distances 100, 200, 500, 800, 1000, 1500, 2000, 3000 and 4000 m.

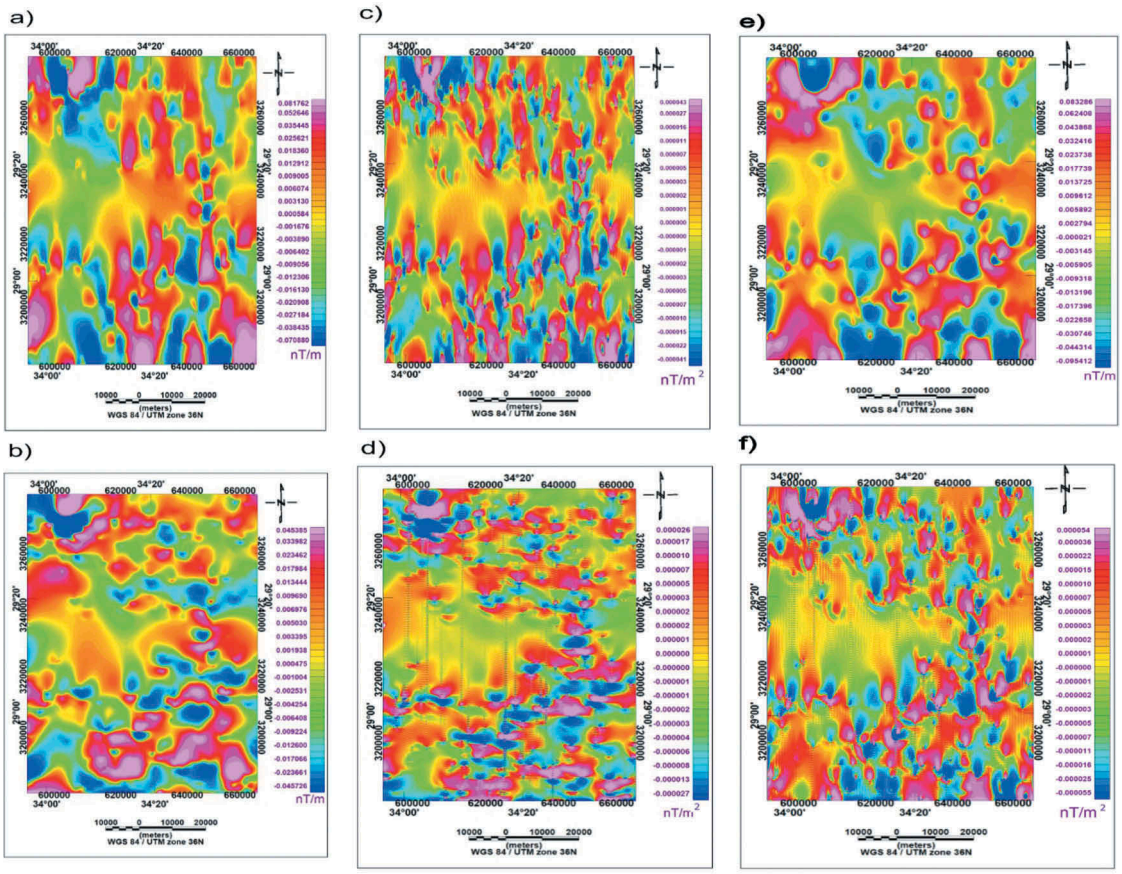

Figure 7. (a) First horizontal derivative of RTP map in X-direction (b) first horizontal derivative of RTP map in y-direction. (c) second horizontal derivative of RTP map in X-direction (d) second horizontal derivative of RTP map in y-direction (e) first vertical derivative of RTP map in z-direction (f) second vertical derivative of RTP map in z-direction.

grid point and the process is repeated for each grid point. If $\Delta g1$, $\Delta g2$, $\Delta g3$, $\Delta g4$ be the anomalies at the stations which are nearest to the station P, then the second vertical derivative at P is given by;

$$\Delta g^{\mathrm{n}} = 4/s\hat{}2(\Delta g - (p - (\Delta g)^{-})) \tag{3}$$

Moreover, the second vertical derivative can be obtained from the horizontal derivative by using Laplace's equation.

$$V^2\mathrm{A} = \frac{\partial^2 \mathrm{A}}{\partial \mathrm{x}^2} + \frac{\partial^2 \mathrm{A}}{\partial \mathrm{y}^2} + \frac{\partial^2 \mathrm{A}}{\partial \mathrm{z}^2} = 0 \tag{4}$$

The second vertical derivative works much the related purpose as "residual" filtering in magnetic maps, in that highlights the expressions of local features, and eliminates the effects of large anomalies or regional magnetism.

As with other derivative exposures, it is un usually effective in the processing step where it can be practised to high light line noise or miss levelling.

4.1.6.1. Vertical derivatives maps. Vertical derivative (first and second) maps (Figure 7(e,f)) were determined from the RTP grid of Nuweiba area.

Vertical derivative enhancements are applied to describe the plan-view boundaries of intra-basement anomalous sources from the data. These two maps sharpened up the anomalies above their sources, and they reduced the complexity of anomalies, providing a distinct imaging of the causative compositions.

The main structural trend in these two maps is the N-S direction.

4.2. Quantitative analysis of the magnetic data

5. 3D magnetic modelling

An interpretation of the magnetic data has been carried by 3-D magnetic modelling by using the GMSYS-3D software. The theoretical background and calculations are performed in the wavenumber domain Parker's algorithm (1972). In this study, the authors used susceptibility 7750 micro CGS for basement rocks. There is conformable between observed and calculate maps, and percentage of error is very small (Figure 8(ac)).

After 3-D modelling, we make basement relief map and 3-D view map (Figure 8(d,e)) which indicates on the basement depth of the studied area. The basement depth has value between 744 m and 4122 m. The depths of basement found in northern, southeastern, southern and central parts of the

studied area are very deep which have values more than 4000 m below the surface which indicate that a thick sedimentary cover, but they decrease gradually in western direction of the area extending from north to south to reach depths have values less than 800 m below the surface.

Results of 3-D magnetic modelling is topographic-depth and basement depth maps (Figure 8(f,g)).

6. Seismic activity

The seismic activity collected in the study for the period 1900–2015, indicates that the fault elements, F2,F6 F7, F8, F12, F14, F15, F16, F17, F18, F19, F20 and F23 detected are active faults where most seismic events are recorded at same sites of these faults especially in the southeastern part of the area under study near the margin of Gulf of Aqba, while F1, F3, F4, F5, F9, F10, F11, F13, F21and F22 are not active faults. The magnitude values are ranging from less 1 to more than 6 on the Richter scale as shown in Figure 9. The seismic activity which are recorded in the area under study have magnitudes values ranging from 1–2 to 5–6 on the Richter scale, and these events were recorded from 1980 to 2015.

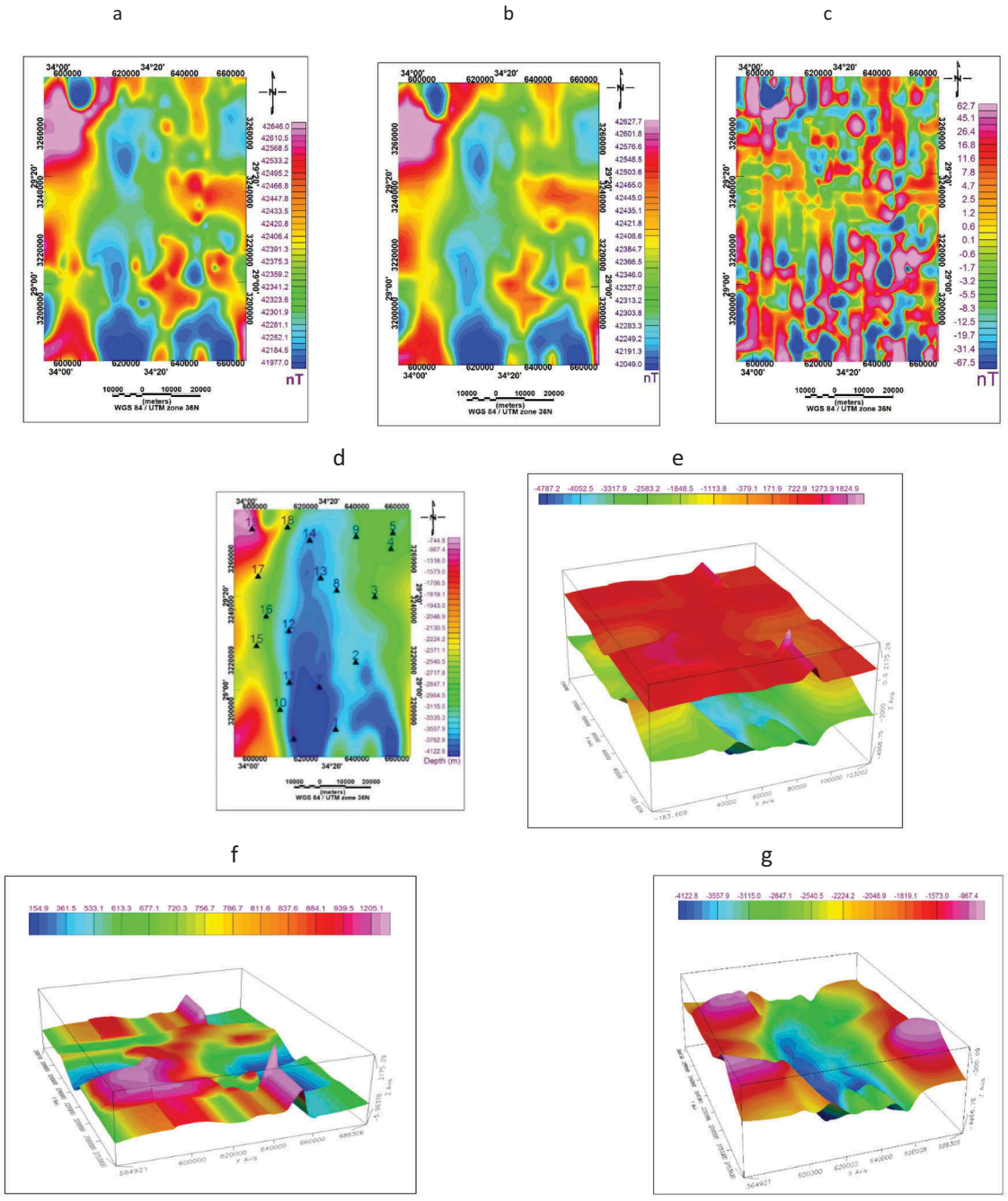

Figure 8. (a) Observed magnetic anomaly, (b) calculated magnetic and (c) error percentage, (d) basement relief map, (e) 3-D view map, (f) Topographic – depth map and (g) Basement – depth map.

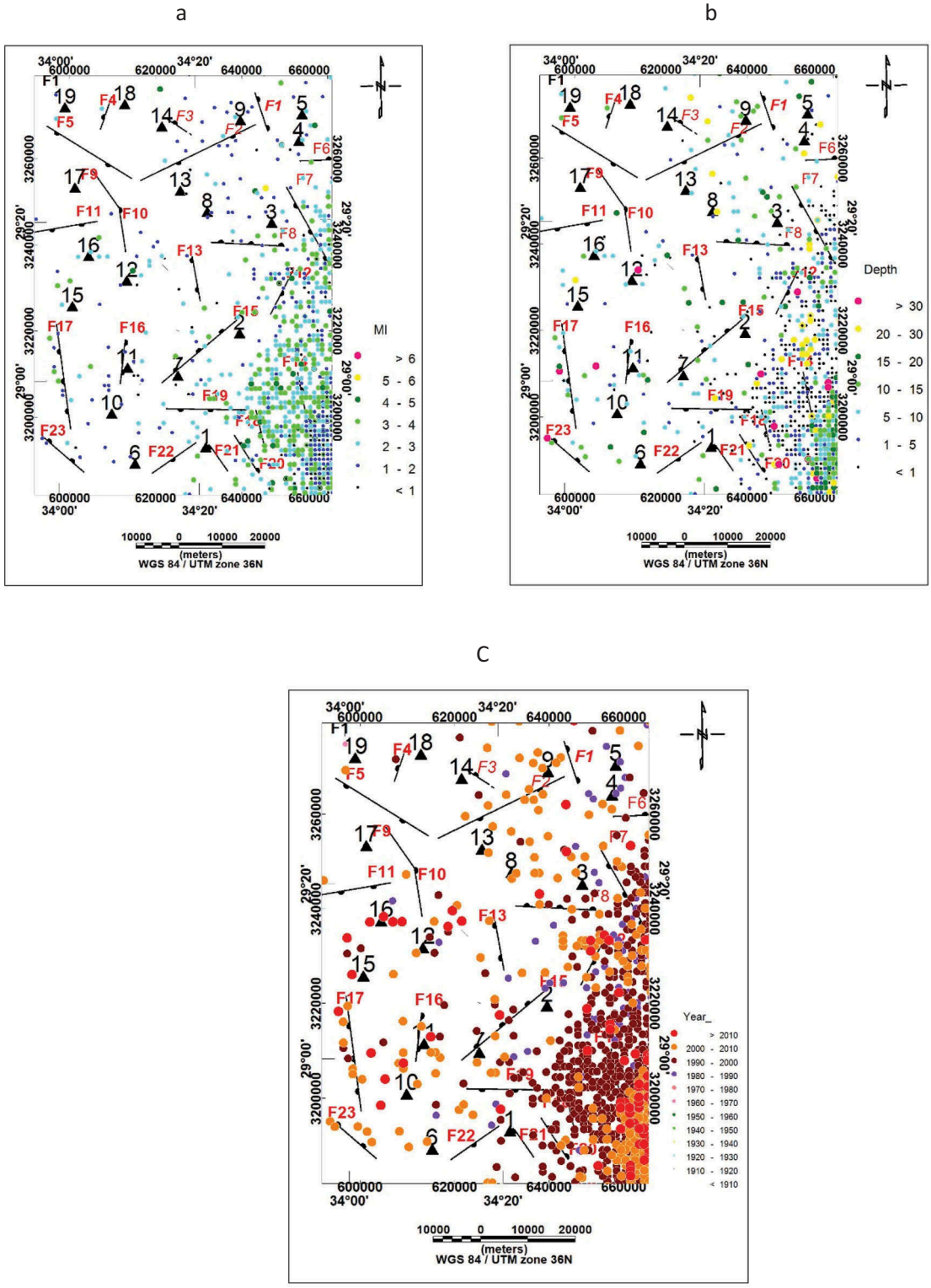

Figure 9. Representation of the seismic activity plotted on fault map constructed from gravity interpretation for (a) magnitude (b) depth of the earthquake and b: date of seismic events from 1900 to 2015.

7. Discussion

Results of the interpretation of gravity and magnetic data have the same trends. The fault elements: F2,F6 F7, F8, F12, F14, F15, F16, F17, F18, F19, F20 and F23 detected are active faults where most seismic events are recorded at same sites of these faults especially in the southeastern part of the area under study near the margin of Gulf of Aqba, while F1, F3, F4, F5, F9, F10, F11, F13, F21and F22 are not active faults as shown in Figure 9. The depth of shallow and deep sources which derived from the spectral analysis 2.7–5.9 Km are identical with results of downward continuation for gravity data where the shallow sources lies between 800 and 1000 m and deep sources lies between 4000 and

5000 m. 3D magnetic modelling indicates that the top of the basement rocks is at a depth of ~ 744 m, which is near the depth of shallow sources determined from the analysis of gravity data. The maximum basement depth from 3-D magnetic modelling is ~4122 m, near the depths of the deep sources determined from the analysis of gravity data.

8. Conclusion

From the integrated geological and geophysical interpretation, we have concluded that the studied area was dissected by many fault elements with strikes oriented N-S, NW-SE (parallel to Gulf of Suez direction), E-W and NE- SW (parallel to Gulf of Aqaba direction). Some of these faults are active faults according to the seismic activity in the study area. Most of the seismic activity in the studied area was recorded after 1980 through 2015. The magnitude of the recorded events ranged from 1–2 to 5–6 on the Richter scale. The depth of basement ranges between 744 and 4122 m from the interpretation of magnetic data. Some parts of the area under study indicate high depth of basement and then more thickness of sedimentary cover which represents the main aquifer for groundwater in the study area.

Disclosure statement

No potential conflict of interest was reported by the authors.

ORCID

Sultan Awad Sultan Araffa http://orcid.org/0000-0002-7098-918X

References

Abdallah AM, Abu Khadrah AM, (1977): Remarks on the geomorphology of the Sinai Peninsula and its associated rock, Egypt. Proceedings, Sixth Colloquium on the Geology of Aegean Region. No. 6; Athens. p. 509–516.

Al Abassy K,A,A. 2010. Geophysical and hydrogeological studies in the area east of Suez Canal, Egypt, msc. Cairo (Egypt): Al-Azhar Uni; p. 183.

Araffa SAS, El Shayeb HM, Hashesh MFA, Hassan NM. 2015. Delineating subsurface structures and assessment of groundwater aquifer using integrated geophysical interpretation at the central part of Sinai, Egypt. Arabian J Geosci. 8(10):7993–8007.

Agah, A. (1981): Structural map and plate reconstruction of the gulf of Suez-Sinai area. Internal Report, Conoco Oil Co., Houston, Texas, USA.

Ball, J. (1916): Geography and geology of west central Sinai. Ministry of Finance and Economy, Survey Department, Cairo, pp. 1–8.

Beadnell, H. J. L. (1927): The wilderness of Sinai. Arnold, London, p 180.

GM-SYS Programs, (2007): Gravity and magnetic modeling, version 6.4.2 (HJ), Inc Suit 500, Richmond St. West Toronto, ON Canada N5SIV6.

Hassanin AM (1997): Geological and geomorphological impacts on the water resources in central Sinai, Egypt [Ph. D. Thesis]. Geol. Dept., Fac. of Sci., Ain-Shams Univ., ARE, p 373.

Hammad, F. A. (1980): Geomorphological and hydrogeological aspects of Sinai Peninsula. Annuals of Geological Survey of Egypt, Vol. X, pp. 807–817.

Ibrahim EH, Shereef MR, El Galladi AA, Pederson LB. 2004. Geoelectric study on quaternary groundwater aquifer in north western Sinai. Egypt EGS J. 2(1):69–74.

Monteiro Santos FAM, Sultan SA, Patricia R, El Sorady AL. 2006. Joint inversion of gravity and geoelectrical data for groundwater and structural investigation: application to the northwestern part of Sinai, Egypt. Geophys J Int. 165:705–718.

Neev D. 1975. Tectonic evolution of the Middle East and the Levantine basin (Easternmost Mediterranean). Geology. 3:683–686.

Oasis Montaj Programs. (2015). Geosoft mapping and processing system: version 8.3.2 (HJ), Inc Suit 500, Richmond St. West Toronto, ON Canada N5SIV6.

Parker RL. 1972. The rapid calculation of potential anomalies, Geophys. J R Astr Soc. 42:315.

Said R, (1990): The geology of Egypt. Published for the Egyptian General Petroleum Corporation, Conoco Hurghada Inc. and Repsal Exploration, S.A, p 734.

Shata, A. 1956: Structural development of Sinai Peninsula, Egypt. Bull. Inst. Desert. Egypt. 6(2):117–157.

Sultan SA, Mekhemer HM, Santos FAM, AbdAlla M. 2009. Ground water exploration and evaluation by using geophysical interpretation (case study: al Qantara East, North Western Sinai, Egypt). Arabian J Geosci. 2:199–211.

Thompson DTT. 1982. Euler, a new technique for making computer assisted depth estimates from magnetic data. Geophysics. 17(47):31–37.

UNSECO Cairo Office. 2005. Geologic map of Sinai, Egypt, scale 1:500,000, project for the capacity building of the Egyptian geological survey and mining authority and the National Authority for remote sensing and space science in cooperation with UNDP and UNSECO. Geological Survey of Egypt, Cairo, Egypt.

Wingograd S. 1978. Computing the discrete fourier transform. Math Comput. 32(141):PP.175–199.

Zaghloul EA. (1983). Reviewon the geology of the northern part of the Gulf of Suez. Total Internal report, Cairo (Egypt).